Production of Cu_2SnS_3 thin films depending on the sulphur flow rate and annealing temperature time

ILHAN CANDAN[1,*], SERAP YIGIT GEZGIN[2], SİLAN BATURAY[1], HAMDİ SUKUR KILIC[2,3,4]
[1]*Department of Physics, Faculty of Science, Dicle University, Diyarbakir, Turkey*
[2]*Department of Physics, Faculty of Science, University of Selcuk, 42031 Selcuklu, Konya, Turkey*
[3]*Directorate of High Technology Research and Application Center, University of Selcuk, 2031 Selcuklu, Konya, Turkey*
[4]*Directorate of Laser Induced Proton Therapy Application and Research Center, University of Selçuk, Konya, Turkey*

Cu_2SnS_3 thin films have been produced using spin coating method for 30 and 40 sccm sulphur flux rate during three annealing times of 15, 30 and 60 minutes at 550 ^oC. Crystal properties, morphological structure, phase structure, elemental contents and optical properties of Cu_2SnS_3 thin films have comprehensively been studied by XRD, SEM, Raman, EDX, UV-vis, and photoluminescence analysis, respectively. The crystalline size, dislocation density, microstrain and crystalline number of Cu_2SnS_3 thin films have been calculated. Cu_2SnS_3-A2 thin film annealed for 30 minutes has the best crystal structure. Cu_2SnS_3 thin films contain four different phases depending on sulphur flux rate and the annealing temperature duration. In addition, their band gaps, extinction coefficients and Urbach energies were determined. The refractive index and high frequency dielectric constant of Cu_2SnS_3 thin film were calculated using Herve and Vandamme, Moss and Ravindra relations and the values found were found to be compatible with one another. The skin depth and optical conductivity of Cu_2SnS_3 thin films were obtained. While the photon energy increased, their skin depth decreased and the optical conductivity considerably increased.

(Received May 11, 2022; accepted April 5, 2023)

Keywords: Cu_2SnS_3, CTS Thin film, Crystalline size, Refractive index, Skin depth

1. Introduction

In recent years, extensive research has been carried out on environmentally friendly and low-cost thin-film solar cells. The thin film solar cells, which are the second-generation solar cells, are produced on active materials such as a-Si, CdTe, $CuInSe_2$ (CIS), $CuInGaSe_2$ (CIGS), Cu_2ZnSnS_4 (CZTS). Among these, CdTe and CIGS materials, which have high efficiency and are commercially produced, are comprising of toxic elements such as Cd and high-cost elements i.e. Te and In. Thus, many studies have been carried out on non-toxic, abundant, low cost CZTS and Cu-Sn-S absorber materials. Cu-Sn-S system has some diverse compositional semiconducting multicomponent phases such as Cu_4SnS_4, $Cu_4Sn_7S_{16}$, Cu_2SnS_3, Cu_3SnS_4 [1]. In the system, Cu_2SnS_3 (CTS) component has some advantages due to lack of Fermi level pinning and its wide stability range. Ternary chalcogenide CTS material is in conductivity of p-type with the tuneable narrow energy band gap between 0.9 and 1.7 eV [2], which has a high coefficient of absorption ($>10^4$ cm^{-1}). CTS is commonly synthesized in phases of cubic, monoclinic and tetragonal. The monoclinic and tetragonal phases are stable structures over a temperature range lower than 750 °C while cubic phase demonstrates a metastable structure over a temperature range higher than 750 ^oC [3].

The world record on the efficiency achieved in CTS thin-film solar cell is 4.29 % for CTS [4,5], 5.24 % for Na doped CTS [6] and 6 % for Ge doped CTS [7]. CTS thin film production technique and process are very important to produce thin film solar cells of CTS with high efficiencies. A number of studies focused on developing relationships between the deposition methods of Cu_2SnS_3 materials and the resulted structure, morphology and electrical conduction. Nevertheless, it is quite challenging to achieve Cu_2SnS_3 in its pure phase of kesterite structure for solar cell applications [8]. Secondary and ternary phases such as Cu_2S, SnS and Cu_3SnS_4 have been obtained during Cu_2SnS_3 synthesis. Moreover, the band gap grading, defects and uncontrolled stoichiometry as well as impurity phases of the secondary or ternary can modify the optoelectronic properties of Cu_2SnS_3 [9]. Many techniques are described to achieve Cu_2SnS_3 thin films, for instance reactive radio frequency magnetron sputtering [8], co-evaporation [9], wet chemical process [10] and spray pyrolysis [11,12]. Nonetheless, merely a limited number of studies have been reported on sprayed Cu_2SnS_3 materials [13]. In comparison to other methods, the Spin coating technique has numerous benefits including low production cost, easy deposition over large-area, and relatively simpler composition adjustment. Therefore, it is particularly more suitable for the thin films' fabrication [14].

Since CTS is a new material for PV field, studies showing the effects of the parameters used, such as sulphur flux and annealing times, in its production of the CTS thin films are very limited in the literature. At this point, information about the characteristic behaviour of CTS thin films is quite insufficient. Therefore, it is a great

need to observe the effect of these parameters on the CTS thin film to produce high quality active layer, especially for obtaining the solar cells with high efficiency as well as other photovoltaic devices.

Considering aforementioned reasons, in this work, CTS thin films were produced for 30 and 40 sccm sulphur flux rate using spin coating method for 15, 30 and 60 minutes annealing durations at 550 ºC temperature, respectively. Analysis of the thin films for the characterisation have been carried out and compared with one another. Thus, we demonstrated the effect of sulphur flow rate and annealing time on CTS thin films during the annealing process and determined the CTS thin films with the ideal active layer property that can be employed in thin film solar cells. To our knowledge, it is the first thorough investigation of CTS thin films produced by spin coating method employing both different sulphur flux and annealing times at a certain temperature. Our results will fill the gap in cutting edge research of CTS thin films structural as well as optical properties and contribute the current research in the literature.

2. Experimental details

In the current work, CTS thin films with different Sulphur flux rate and time were fabricated on soda lime glass substrate using a solution comprising 0.389 g copper (II) acetate ($Cu(CH_3COO)2{\cdot}H_2O$), 0.220 g tin (II) chloride dehydrate ($SnCl_2.2H_2O$) and 0.444 g thiourea (CH_4N_2S) deposited under optimized conditions. All chemicals are separately dissolved in mixing of ethanol and glacial acetic acid for 6 h at room temperature in magnetic stirring. Firstly, thiourea solution was slowly mixed into the copper (II) acetate solution, then, tin (II) chloride dehydrate was poured into the thiourea/copper (II) acetate solution. Finally, obtained solutions were stirred at room temperature for 4 h until a homogenous clear solution was obtained. To regulate pH values, a few drops of diethanolamine were added to the mixed solution for the final solution. The molar ratios of the Cu/Sn/S elements in the solutions were 2/1/6. Thiourea has volatile nature at high temperature [15]. Therefore. This was added twice to avoid the possible loss of sulphur.

Before deposition process, the glass substrates were washed by boiling in sufficient quantities of a mixture of H_2O, NH_3, and H_2O_2 at 105 °C and then, in sufficient quantities of a mixture of H_2O, H_2O_2, and HCl at 105 °C to eliminate any residual waste. Then, the glass substrates were cleaned in deionized water for 3 min. each and later dried. After obtaining the final solutions and cleaning the substrates, the obtained solution was deposited via spin coating at a rate of 1500 rpm for 63 s in air. The final solutions were deposited onto the glass substrate layer by layer, and each layer was preheated to 220 °C for 10 min. After this process, obtained films annealed under 30 and 40 sccm in 10 % H_2S + 90 % Ar atmosphere at 550 °C temperature in furnace. CTS thin films were annealed under 30 sccm 10 % H_2S + 90 % Ar atmosphere at 550 °C temperatures for 15, 30 and 60 min. and 40 sccm 10 % H_2S + 90 % Ar atmosphere at 550 °C temperatures for 15, 30 and 60 min., respectively. The obtained sample names are demonstrated in Table 1 with Sulphur flux rate and time.

The effect of Sulfurization effect on the structural, morphological, optical and photoluminescence properties of CTS thin film are studied in this work. The crystalline properties of the acquired CTS film were studied by X-Ray Diffractometer (XRD) unit (Bruker D8 Advance) operated at 40 kV and 40 mA. XRD is set up with the range of θ-2θ in the steps of 0.02º to analyse structural and phase purity analysis of the CTS thin film structure. In addition, the obtained films were analysed using Confocal Raman Microscope. The surface topology and EDX measurements of all obtained films were obtained by FEI Quanta 250 FEG Scanning Electron Microscopy (FEI Co., Eindhoven, Netherlands). The conclusions of the transmittance, energy band gap and Urbach energy of the thin films were analysed by Shimadzu UV-3600 spectrophotometer (Shimadzu, Tokyo, Japan) between 300-1100 nm.

Table 1. Fabrication parameters for CTS film

Thin films	Sulphur annealing temperature and time	Sulphur flux rate
CTS-A1	550 °C for 15 min	30 sccm H2S:Ar
CTS-A2	550 °C for 30 min	30 sccm H_2S:Ar
CTS-A3	550 °C for 60 min	30 sccm H_2S:Ar
CTS-B1	550 °C for 15 min	40 sccm H_2S:Ar
CTS-B2	550 °C for 30 min	40 sccm H_2S:Ar
CTS-B3	550 °C for 60 min	40 sccm H_2S:Ar

3. Results and discussions

3.1. XRD analyses

CTS-A and CTS-B thin films have been determined for having predominantly tetragonal Cu_2SnS_3 and orthorhombic Cu_3SnS_4 crystal structures, as seen in XRD and Raman Spectra in Fig. 1(a-b). It can be seen that their orientations are in (112/222), (200/040), (220/044) and (312/262) crystalline planes formed on 2θ=28.8º, 33.3º, 47.6º, 56.4º angles, respectively. In addition, when the sulphur flow rate was increased to 40 sccm, the second phases [16-21] in CTS-B thin films [1, 22-25] were formed on 2θ=27.7º and 31.0º angles.

The crystal properties of CTS-A thin film were improved, as the annealing duration was increased from 15 minutes to 30 minutes at 30 sccm sulphur flow rate since the sulphur vapour pressure was increased [26]. It is concluded that CTS-A2 thin film annealed for 30 minutes has the best crystal structure. However, when the annealing duration is increased to 60 min, the crystal structure weakens due to over annealing. When the sulphur flow rate was increased to 40 sccm, Sn and S atoms were reacted to form SnS phase in surface of CTS-B thin film due to high sulphur rate. In addition, the inability of Cu, Sn and S atoms to align properly in the crystal

structure at high sulphur flow rate may cause a Cu_4SnS_4 phase to be formed. Moreover, CTS-A thin films produced at 30 sccm of sulphur flux indicated a better crystal structure than that of CTS-B thin films produced at 40 sccm of sulphur flux. The second phase formations slightly distorted the crystal structure of CTS-B thin films compared to CTS-A thin films [27]. In addition, at high sulphur flow rate, the diffusion action of Sn atoms may disrupt the XRD structure [28]. CTS-A2 thin film has a good crystal structure for 30 min. annealing time at 30 sccm sulphur flux rate. For 40 sccm of sulphur flux, the crystal structures of CTS-B thin films did not show any significant changes among themselves.

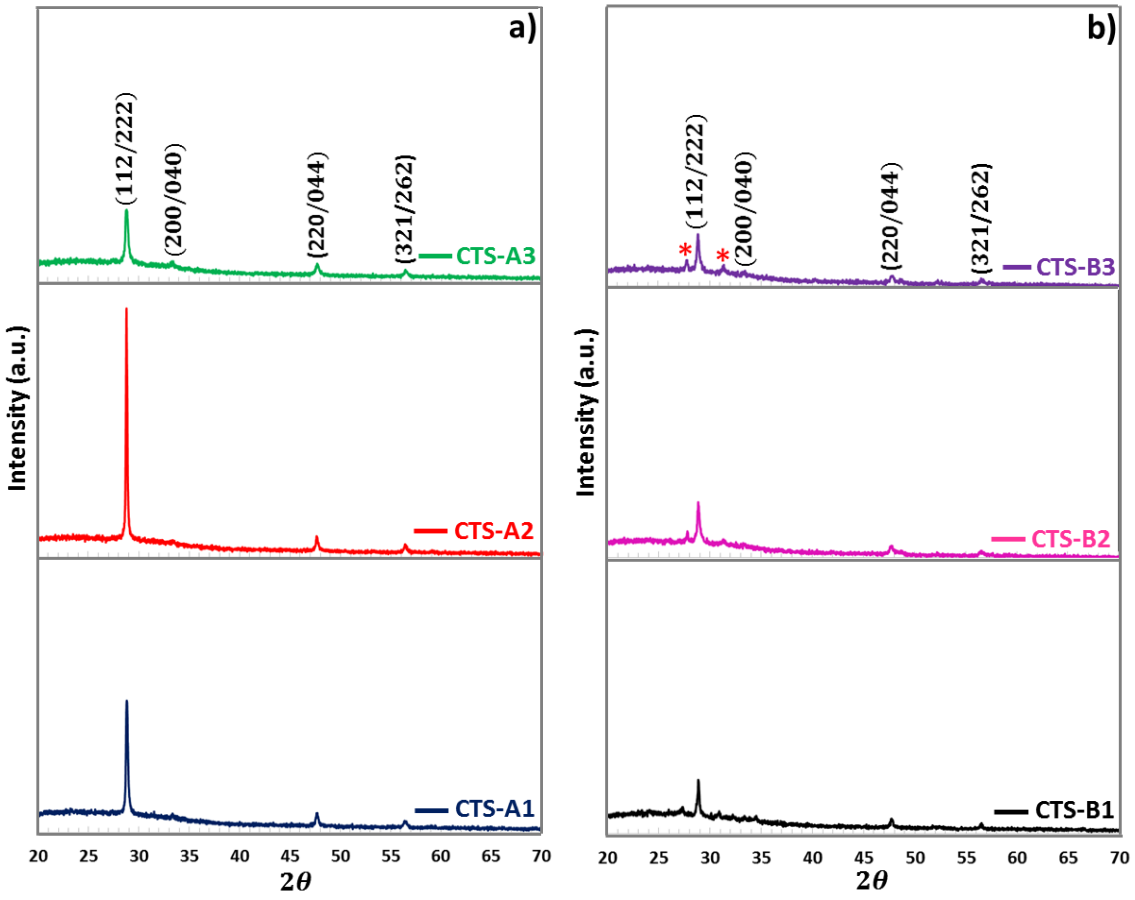

Fig. 1. XRD patterns of produced a) CTS-A and b) CTS-B thin films (color online)

The crystal sizes of CTS films are calculated by Scherer equation:

$$D = 0.94\lambda/\beta cos\theta \quad (1)$$

where D, λ, β and θ parameters are the size of crystalline, X-Ray wavelength, the diffraction peak's full-width at half-maximum, and angle of Bragg diffraction, respectively. The main crystalline sizes of CTS-A1, CTS-A2, CTS-A3, CTS-B1, CTS-B2 and CTS-B3 thin films have been determined to be 42.85, 55.56, 34.28, 40.81, 35.71 and 32.96 nm, respectively. CTS-A2 thin film has the enlarge crystal size while CTS-B3 has the lowest crystal size. In addition, when the annealing time enhanced, the crystalline sizes of CTS-B thin films decreased for 40 sccm sulphur flux rate.

The thin films' dislocation density and micro-strain are determined by Equation (Eq) (2) and Eq (3) as following:

$$\delta = \frac{1}{D^2} \quad (2)$$

$$\varepsilon = \frac{\beta cos\theta}{4} \quad (3)$$

The dislocation density (δ) and micro strain (ε) of CTS-A and CTS-B ultrathin films express the defect and trap formations in the thin film and negatively affect the crystal structure, respectively. The smallness of these two parameters is an indication of development of the crystal structure. According to that statement, the small dislocation density and micro-strain values of CTS-A2 thin film compared to the others indicate that its crystal structure is better developed and the less lattice defect numbers are taken place [29, 30]. Moreover, for 40 sccm of sulphur flux, dislocation density and micro-strain enhancement with some increase in the duration of annealing process were recorded. Some improvements in the CTS-A2 thin film's crystal structure allow a better

transmission of minority charge carriers in CTS solar cell's absorber layer. Thus, the series resistance of the solar cell is decreased, and thus, its PV performance is more enhanced.

Table 2. Crystalline size, dislocation density and micro-strain of CTS-A and CTS-B thin films [12]

Ultrathin films	*Crystalline Size (nm)*	*Dislocation Density* $\times 10^{16}$ *(lines/m²)*	*Micro-strain* $\times 10^{-3}$	*Crystalline Number* $\times 10^{16}$ *(m⁻²)*
CTS-A1	42.85	5.45	0.84	1.27
CTS-A2	55.56	3.24	0.65	0.58
CTS-A3	34.28	8.51	1.05	2.48
CTS-B1	40.81	6.02	0.88	1.47
CTS-B2	35.71	7.84	1.01	2.20
CTS-B3	32.96	9.21	1.09	2.79

The number of crystals per unit surface area (N) is expressed by Eq (4),

$$N = \frac{T}{D^3} \tag{4}$$

where T is thin film thickness. As seen in Table 2, CTS-A2 thin film has the lowest crystalline number among all the thin films, which were caused by the larger crystal size of the CTS-A2 thin film. Conversely, CTS-B3 with the smallest crystal size contains the lower crystal numbers [31].

3.2. Raman analyses

Raman spectrum in Fig. 2 (a-b) presents a number of phase structures developed in CTS-A and CTS-B thin films over 200-450 cm^{-1} wavenumber range at room temperature. CTS thin films contain four different CTS phases depending on sulphur flux rate and the annealing temperature duration. CTS-A thin films annealed under 30 sccm sulphur flow which show the modes based on monoclinic (254 [32], 291 [1], 372 cm^{-1} [1, 33, 34]), tetragonal (297 [1, 35, 36], 320 [1, 37], 351 cm^{-1} [1, 35, 36]) Cu_2SnS_3 and orthorhombic Cu_3SnS_4 (317 cm^{-1} [38, 39]) phases. CTS-B thin films annealed under 40 sccm sulphur flow which have Raman peaks of SnS phase (224 cm^{-1}) [16, 40, 41], monoclinic Cu_2SnS_3 (254, 372 cm^{-1}), Cu_2SnS_3 tetragonal (293 [1], 296 [1], 320 , 344 cm^{-1} [1]), orthorhombic Cu_4SnS_4 (315 cm^{-1} [1]) and Cu_3SnS_4 (318 cm^{-1} [42-44]) phases. For the 30 min. annealing time interval, the CTS-A2 thin film shows the most intense peak on 319 cm^{-1}, while the CTS-B2 thin film indicates the strongest peaks on 293 and 351 cm^{-1}. Thus, the predominantly tetragonal phase formations in Raman spectra confirm that the CTS-A and CTS-B thin films are formed in the tetragonal crystal structure.

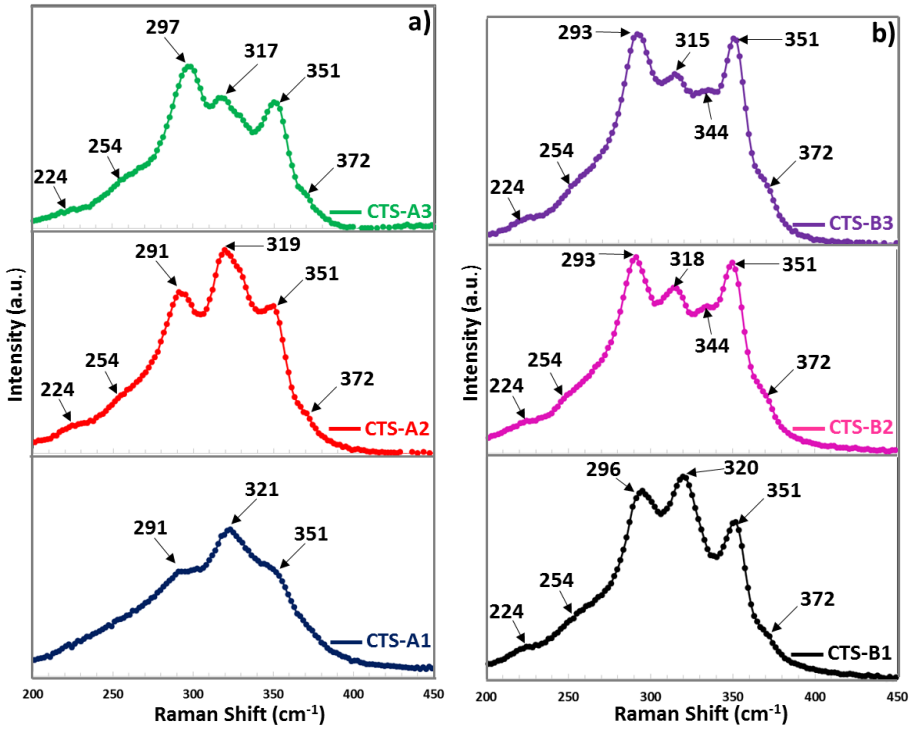

Fig. 2. Raman Spectra of a) CTS-A and b) CTS-B thin films (color online)

3.3. Photoluminescence analyses

The photoluminescence spectra of CTS-A thin films and CTS-B thin films are shown in Fig. 3(a-b), respectively. All the samples indicate emission between 860 and 920 nm. Luminescence was detected at 1.40 eV (881 nm) under excitation. PL intensity of CTS-A2 and CTS-B1 thin films are lower compared to other CTS-A and CTS-B thin films, respectively. This decrement in excitation power is based on the band-to-band transition and non-radiative recombination in CTS thin film [45]. Furthermore, the possibility of reabsorption in thin films may cause PL intensity to decrease [46]. Therefore, there is some differences between the band gaps and PL energies of CTS thin films.

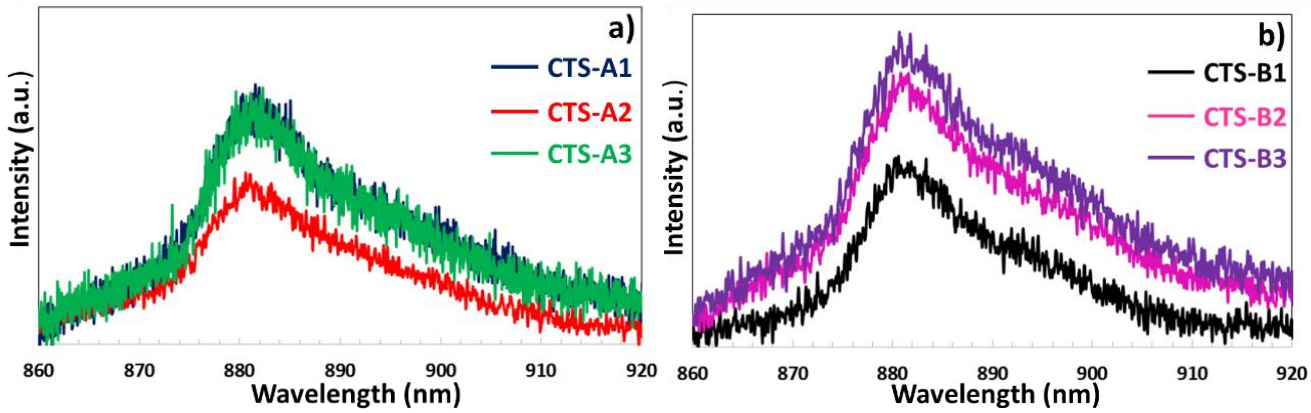

Fig. 3. Photoluminescence spectra of a) CTS-A and b) CTS-B thin films (color online)

3.4. Morphologic analyses

According to the SEM images in Fig. 4 (a-f), the particle size reduction occurred when annealing time duration was raised from 15 to 30 min. at low sulphur flow rate (30 sccm). It can be noticed that a small decrease in the amount of Sn can cause the particle size to decrease. The Average grain size of the CTS layers for SEM analysis ranges from 163 to 246 nm. In addition, when the annealing time was increased to 30 min., the larger particles could be fragmented into smaller sized particles [47]. Contrary to this situation, when the time of annealing was changed to 60 min, it was observed that the particle size was increased. It has similarly been noticed that particles are coalesced and regrown at 60 min. annealing time duration. However, when the sulphur flux rate was increased, the particle growth deteriorated. In particular, there was a spongy growth consisting of tiny particles on the CTS-B2 and CTS-B3 thin films [48], and large particles were formed on it. Furthermore, when the annealing time is increased, the significant decrease in the amount of Sn and the diffusion mobility of Sn atoms can cause deterioration in the morphology of the thin film [27]. This confirms the second phase formations in CTS-B thin films [17, 27], and the crystal structures of these thin films decrease as the annealing duration increases. However, the high annealing temperature at high sulphur flux can cause region-by-region large particle growths [26, 48].

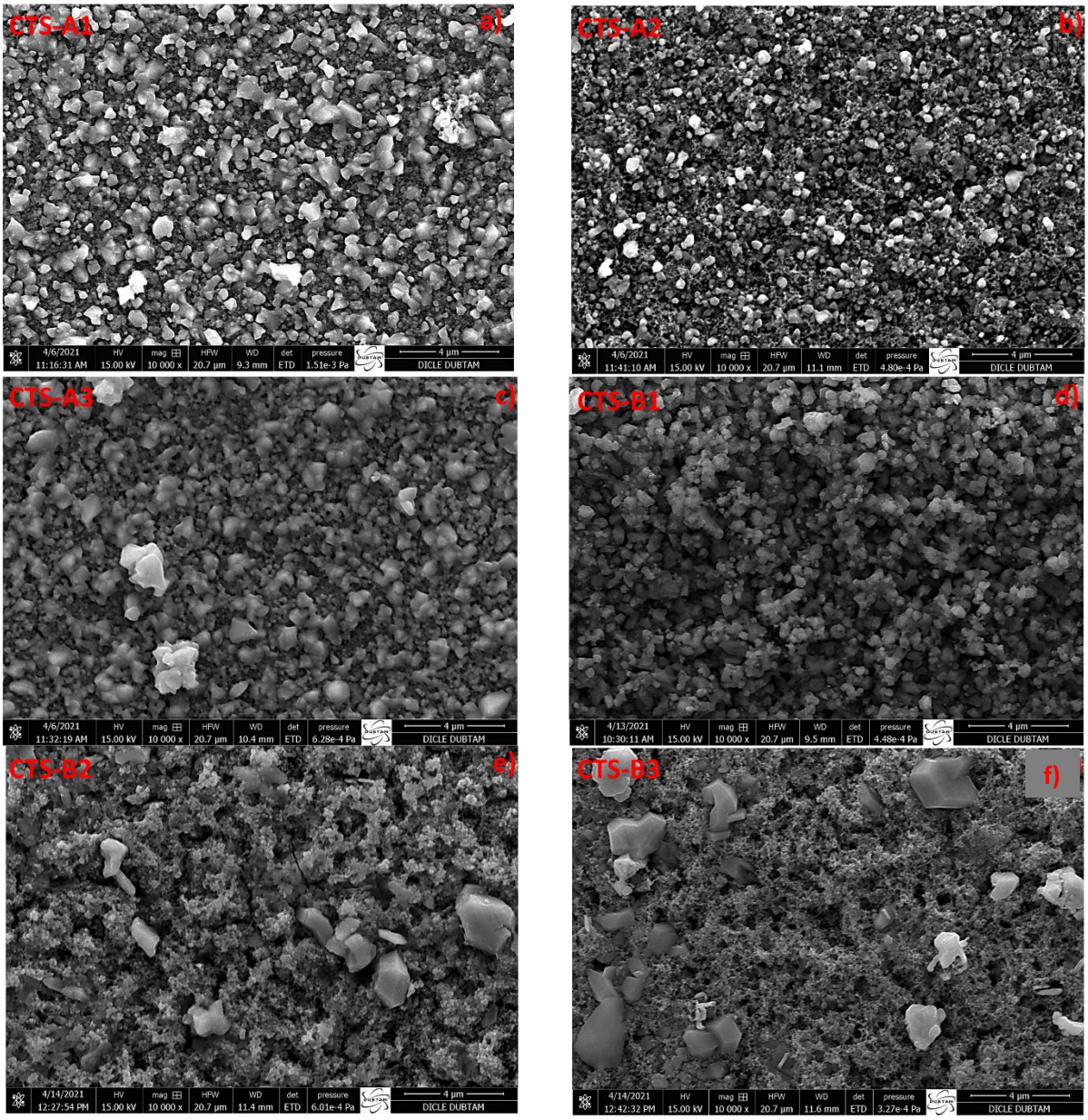

Fig. 4. SEM images of (a, b, and c) CTS-A and (d, e, and f) CTS-B thin films (color online)

3.5. EDX analyses

As seen in the EDX spectrum in the Fig. 5(a, b, and c) and in Table 3, CTS-A thin film are Cu poor and Sn rich. The sulphur flow rate and the annealing time duration affect the composition of CTS thin film. Copper vacancies (V_{cu}), which are dominant acceptor defect, improve the p-type conductivity of CTS thin film. As the annealing time duration is increased, the amount of Cu increases and the amount of Sn decreases. V_{Cu} defects enhance the performance of the solar cell. Additionally, Sn_{Cu} donor defects occur when Sn occupy the Cu vacancies [28, 49], which can act as a recombination centre. Although CTS-B1 thin film is Cu poor and Sn rich, CTS-B2 and CTS-B3 thin films are Cu rich and Sn poor on the contrary, as shown in Fig. 5(d, e, and f). That is because, the sulphur content strongly depends on the annealing time at a high sulphur flow rate. As the annealing time increases, the amount of tin element decreases. This situation can be attributed to the evaporation of the element Sn at the high annealing time duration [47].

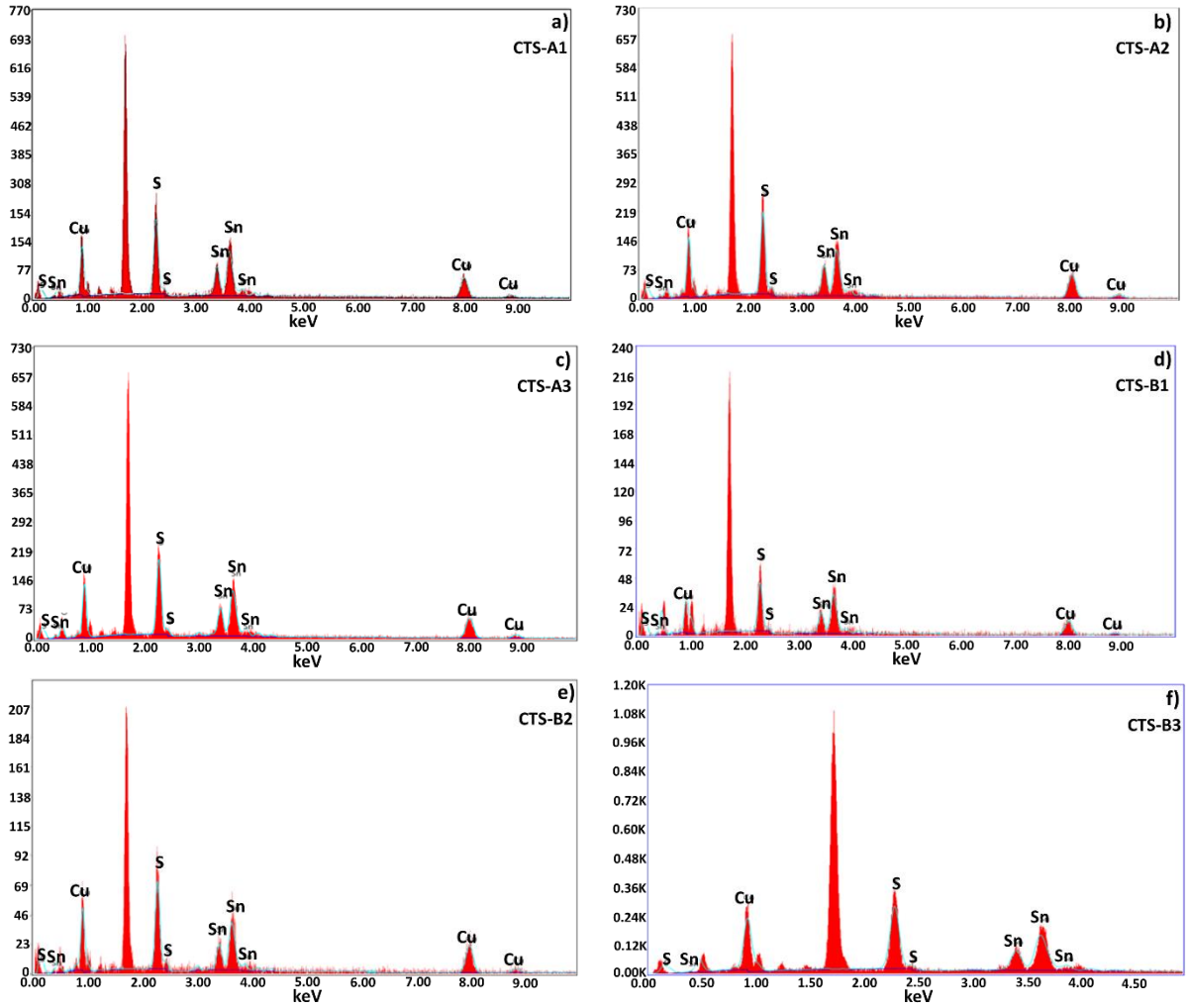

Fig. 5. EDX Spectra of (a, b, and c) CTS-A and (d, e, and f) CTS-B thin films (color online)

Table 3. The rates of elements in CIGS-1, CIGS-2, CIGS-3 and CIGS-4 ultrathin films

Ultrathin films	***Cu(%)***	***Sn(%)***	***S(%)***	***Cu/Sn***	***S/metal***
CTS-A1	24.46	15.93	59.61	1.53	1.47
CTS-A2	25.65	15.25	59.10	1.68	1.44
CTS-A3	26.55	15.07	58.38	1.76	1.40
CTS-B1	25.83	16.26	57.50	1.58	1.36
CTS-B2	28.32	12.49	59.20	2.26	1.45
CTS-B3	28.03	13.00	58.97	2.15	1.43

3.6. Optical analyses

The Tauc equation is used to calculate the band gap of thin films and expressed as:

$$\alpha h\nu = A\left(h\nu - E_g\right)^{1/2} \tag{5}$$

where $h\nu$ is the energy of photon, Eg is thin film band gap, A is a constant. Eg is obtained by straight line of $(\alpha h\nu)^2$ versus $(h\nu)$ in Tauc plot in Fig 6a and 6b. The band gaps of CTS-A1, CTS-A2, CTS-A3, CTS-B1, CTS-B2 and CTS-B3 have been calculated to be 1.55, 1.12, 1.59, 1.42, 1.22, and 1.37 eV, respectively. For 30 min. annealing time, CTS-A2 and CTS-B2 thin films have the lowest band gaps.

The refractive index (n) of the semiconductor is an important parameter that affects the performance of the solar cell. The calculation of refractive index is performed based on the band gap using Moss relation in Eq (6):

$$E_g n^4 = k \tag{6}$$

where k is a constant, which is 108 eV. Similarly, the relation between n and E_g is expressed by Eq (7) employing Herve and Vandamme as following[31];

$$n = \sqrt{1 + \left(\frac{A}{E_g + B}\right)^2} \quad (7)$$

where A and B are constants and have values of 13.6 and 3.4 eV, respectively. In addition to the Moss and Herve and Vandamme relations, Ravindra defined interest between the refractive index and E_g, using Eq (8) [50].

$$n = 4.16 - 0.85E_g \quad (8)$$

The refractive index of CTS-A and CTS-B thin films found using Eqs. (6), (7) and (8) are shown in Table 4. The refractive indexes were determined by Herve and Vandamme, Moss and Ravindra relations which do not significantly diverge. According to these three relations, while the band gaps of the thin films decrease, their refractive indices upsurge. In particular, the CTS-A2 thin film's high refractive index can be attributed to improved crystalline structure and thin film densification [51].

The dielectric coefficient is a factor expressed by the electric field between charges in thin film semiconductor and it is an important parameter that determines the charge accumulation in the solar cell. In this study, the values of high frequency dielectric constant (ε_∞) and the static dielectric constant (ε_o) were calculated by using Eq (9) and Eq (10), respectively[31]:

$$\varepsilon_\infty = n^2 \quad (9)$$

$$\varepsilon_o = 18.52 - 3.08E_g \quad (10)$$

Between all CTS thin films, CTS-A2 and CTS-B2 thin films have higher dielectric coefficients, which can lead to facilitate charge transitions, increase the lifetime of the charges and stabilizes the charge mobility in thin films [52].

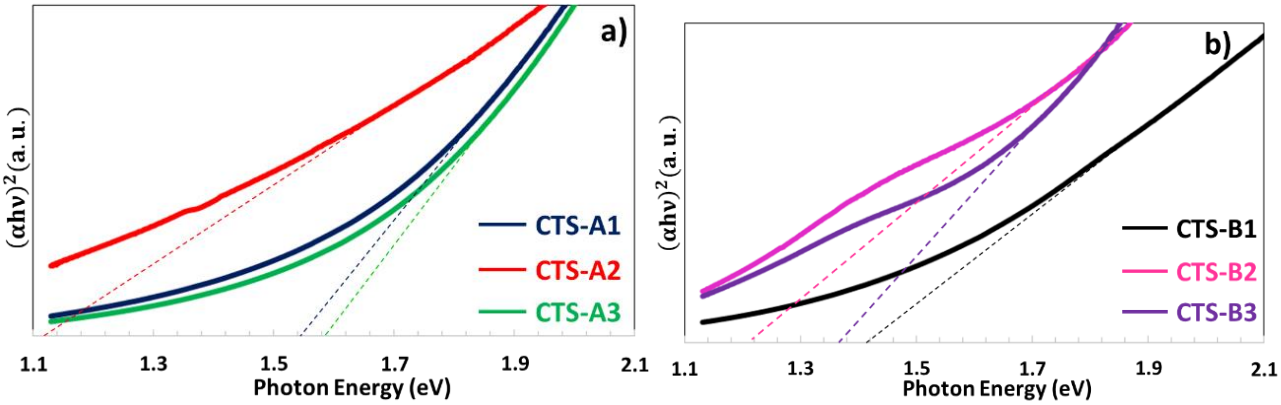

Fig. 6. Tauc plots of a) CTS-A and b) CTS-B thin films (color online)

Table 4. Refractive index (n), high frequency dielectric constant (ε_∞) and static dielectric constant (ε_o) of CTS-A and CTS-B thin films

Samples	E_g (eV)	Moss relation		Herve&Vandemme		Ravindra		Static Dielectric Constant, ε_o
		n	ε_∞	n	ε_∞	n	ε_∞	
CTS-A1	1.55	2.89	8.35	2.92	8.52	2.84	8.06	13.75
CTS-A2	1.12	3.13	9.80	3.17	10.04	3.20	10.24	15.07
CTS-A3	1.59	2.87	8.23	2.90	8.41	2.80	7.84	13.62
CTS-B1	1.42	2.95	8.70	2.99	8.94	2.95	8.70	14.15
CTS-B2	1.22	3.06	9.36	3.10	9.61	3.12	9.73	14.76
CTS-B3	1.37	2.97	8.82	3.02	9.12	2.99	8.94	14.30

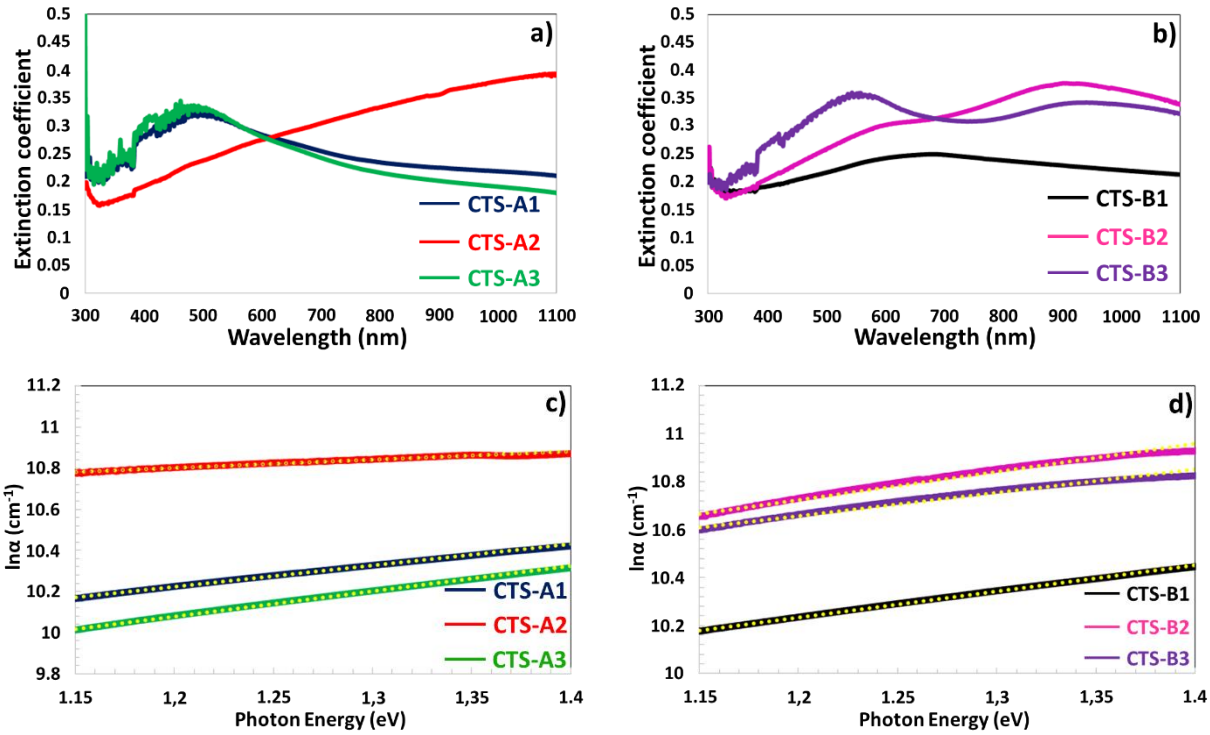

Fig 7. The extinction coefficient and Urbach energy of (a and c) CTS-A and (b and d) CTS-B thin films, respectively (color online)

The light lost becaue of absorption and scattering is determined by the extinction coefficient. The extinction coefficient (k) is represented by Eq (11):

$$k = \frac{\alpha\lambda}{4\pi} \tag{11}$$

where α is the coefficient of absorption, λ is the wavelength of the light. The absorption coefficient is expressed by $\alpha = 2.303(A/T)$ equation[31]. In this equation, T is the thin film thickness and A is the absorbance of the material. The average thickness of CTS thin films is 1 µm with negligible differences among all CTS thin films. In our study, we carried out the measurements at constant temperature of 550 °C. But one would expect that as the temperature varies, thickness of the CTS films changes. If the annealing temperature increases, thickness of the CTS films should increase. As seen in the extinction spectrum in Fig 7a, CTS-A1 and CTS-A3 thin films have higher extinction coefficient while the extinction coefficient of CTS-A2 thin film increases when moved from UV to the near infrared region. CTS-B1 thin film has lower extinction coefficient than other thin films for all spectral regions. The extinction coefficient of CTS-B3 is enhanced over the wavelength region of 500-600 nm while CTS-B2 has higher extinction coefficient for the near infrared wavelength region as seen in Fig 7b.

Urbach energy (E_U), or band tail width, is used to determine the degree of disorder in low crystalline materials as well as amorphous materials. Due to the phonon interactions, the band tailing formation in the band gap is initiated by impurities in the semiconductor. Urbach energy expresses material disorder corresponding to transitions between localized states of the conduction band and extended states of valance band. By using Eq (5), the disorder in the compound can be projected from the change in the coefficient of absorption (α), by Eq (12) as given below:

$$\alpha = \alpha_o exp(h\nu/E_U) \tag{12}$$

α_o is a constant, E_U is expressed to be the tail width of localized states in the band gap. E_U was acquired by determining the slope of ($ln\alpha$) versus ($h\nu$) shown in Fig 7c and 7d [30]. As seen in Fig 8a, the band gaps of CTS-A and CTS-B thin films are inversely proportional to their E_U energy. However, according to Fig 8b, E_U energies CTS-B thin films, which is directly proportional their band gaps. Except for CTS-A2, all other CTS thin films have E_U energies below their band gap. Although the CTS-A2 thin film has the lowest band gap, it has the highest Urbach energy which can be attributed to stoichiometric deviation, the distortion in the film expanding the band tail and the localized states [53, 54].

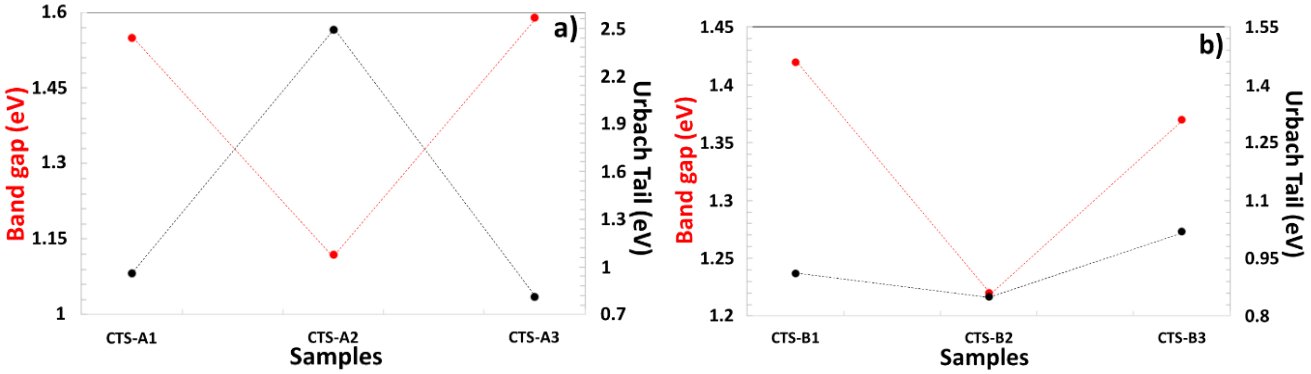

Fig 8. The relation between the optical band gap and the Urbach energy of a) CTS-A and b) CTS-B thin films (color online)

Skin depth (χ) refers to the distance at which light is penetrated through the thickness of the thin film. Skin depth of CTS thin films that is calculated using Eq (13);

$$\chi = \frac{\lambda}{2\pi k} \tag{13}$$

The Fig. 9a and 9b show the change in χ values of CTS-A and CTS-B thin films as a function of wavelength, respectively. The skin depth of CTS thin films decreased while the photon energy increased [31]. CTS-A2 thin film has a lower and higher skin depth in the low and high energy region compared to other CTS-A thin films, respectively. Because the CTS-A2 thin film has a larger crystalline size, it limits the transmission of light in the energy region. Besides, CTS-B1 thin film indicates skin depth in the energy range of 1-3 eV compared to other CTS-B thin films. The fact that the CTS-B2 and CTS-B3 thin films are composed of large particles in certain regions can prevent the light transmission of these thin films in this range.

The role of skin depth in the CTS solar cell is quite important. As skin depth increases, the electron hole pairs rise as well. On the other hand, if the skin depth decreases, the electron hole pairs would decrease accordingly.

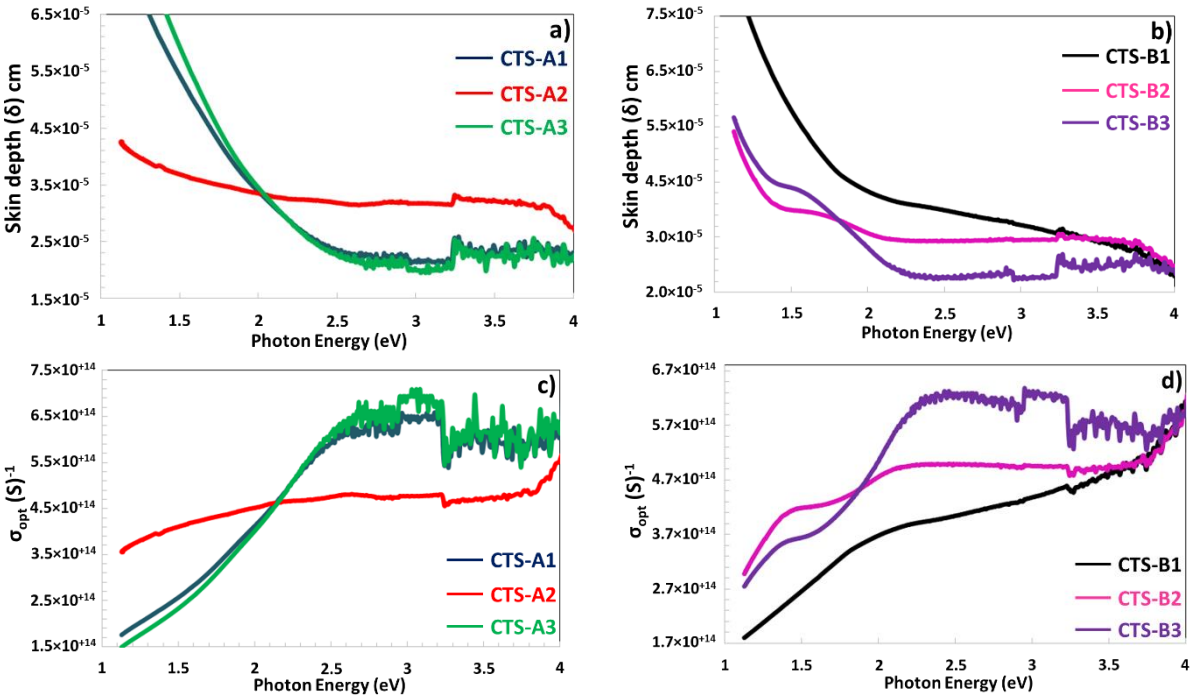

Fig 9. Skin depth and optical conductivity of (a and c) CTS-A and (b and d) CTS-B thin films (color online)

The optical conductivity of CTS thin films is determined using Eq (14);

$$\sigma_{opt} = \frac{\alpha n c}{4\pi} \tag{14}$$

where c is the light speed. The optical conductivity determines the density of photo excited electrons [53, 55]. According to Fig. 9c, CTS-A2 thin film shows a higher optical conductivity in the low energy region compared to the others. Moreover, CTS-A1 and A3 thin films have

lower and higher photo excited electrons in the low energy and higher energy region, respectively. The optical conductivity is the lower in CTS-B1 thin film. CTS-B3 thin film has higher electrons excitation by the higher photon energy. However, the optical conductivity of all CTS-A and CTS-B thin films enhances with increasing the photon energy as shown in Fig. 9 (c and d).

4. Conclusions

CTS thin films were produced for 30 and 40 sccm sulphur flux rates in 15, 30 and 60 minutes annealing time durations at a constant 550 ºC temperature. CTS thin films have tetragonal Cu_2SnS_3 and orthorhombic Cu_3SnS_4 crystalline structures. CTS-B thin films produced under 40 sccm sulphur flux have the second phases. Among thin films, CTS-A2 thin film has the most improved crystal structure and its crystal size and crystalline number were determined to be 55.56 nm and 0.58×10^{16} m^{-2}, respectively. While CTS-A thin films produced at 30 sccm sulphur flux contain monoclinic and tetragonal Cu_2SnS_3 phase and orthorhombic Cu_3SnS_4 phase, CTS-B thin films at 40 sccm sulphur flux include orthorhombic Cu_4SnS_4 and SnS phases in addition to these phases. CTS thin films have band gaps between 1.12 and 1.59 eV. The band gaps of CTS-A1, CTS-A2, CTS-A3, CTS-B1, CTS-B2 and CTS-B3 have been calculated to be 1.55, 1.12, 1.59, 1.42, 1.22, and 1.37 eV, respectively. For 30 min. annealing time, CTS-A2 and CTS-B2 thin films have the lowest band gaps.

The refractive index and high frequency dielectric constant of CTS thin film were calculated using Moss, Herve and Vandamme and Ravindra relations and the values were found to be compatible with each other. The extinction coefficient of CTS-A2 thin film increased towards the higher wavelength region compared to other CTS-A thin films. However, among CTS-B thin films, the extinction coefficient was relatively lower in all regions compared to the others. It was found that the band gaps of CTS thin films were inversely proportional to their Urbach energies. While the photon energy increased, CTS thin film's skin depth decreased and their optical conductivity increased.

Although the crystal structure of the CTS-A2 thin film is the most advanced among all other thin films, it is slightly different in optical properties compared to the others. This situation can be attributed to partial morphological disorder and stoichiometric deviation. With the improvement work to be carried out, solar cells can have the most ideal properties to be employed as active layer in future work.

Acknowledgements

Authors wish to kindly thank the following funding bodies for their support.

- Selcuk University Scientific Research Project (BAP) Coordination for the support with the number 15201070 and 19401140 projects.
- Selçuk University, High Technology Research and Application Center (İL-TEK) and SULTAN Center for infrastructures.
- Dicle University Scientific Research Project (BAP) Coordination for the support with the number FEN.18.007 project.

References

[1] V. R. Reddy, M.R. Pallavolu, P. R. Guddeti, S. Gedi, K. K. Reddy, B. Pejjai, W. K. Kim, T. R. Kotte, C. Park, Ind. Eng. Chem. **76**, 39 (2019).
[2] S. Rahaman, M. K. Singh, M. A. Sunil, K. Ghosh, Superlattices Microstruct. **145**, 106589 (2020).
[3] A.C. Lokhande, R.B. Chalapathy, M. He, E. Jo, M. Gang, S. A. Pawar, C. D. Lokhande, J. H. Kim, Sol. Energy Mater Sol. Cells **153**, 84 (2016).
[4] A. Kanai, K. Toyonaga, K. Chino, H. Katagiri, H. Araki, Jpn. J. Appl Phys. **54**(8S1), 08KC06 (2015).
[5] S. Y. Gezgin, A. Kepceoğlu, H. Ş. Kılıç, AIP Conference Proceedings **1815**(1), 030019 (2017).
[6] A. Kanai, M. Sugiyama, Sol. Energy Mater Sol. Cells. **231**, 111315 (2021).
[7] M. Umehara, Y. Takeda, T. Motohiro, T. Sakai, H. Awano, R. Maekawa, Appl. Phys. Express. **6**, 045501 (2013).
[8] J. Zhou, L. You, S. Li, Y. Yang, Mater. Lett. **81**, 248 (2012).
[9] Z. Seboui, A. Gassoumi, N. Kamoun-Turki, Mater. Sci. Semicond. Process. **26**, 360 (2014).
[10] K. Tanaka, Y. Fukui, N. Moritake, H. Uchiki, Sol. Energy Mater Sol. Cells. **95**, 838 (2011).
[11] K. Woo, Y. Kim, J. Moon, Energy Environ. Sci. **5**, 5340 (2012).
[12] S. Yiğit Gezgin, İ. Candan, Ş. Baturay, H. Ş. Kılıç, Middle East J. Sci. **8**(1), 64 (2022).
[13] Y. Wang, H. Gong, J. Alloys Compd. **509**, 9627 (2011).
[14] S. Rabaoui, H. Dahman, N. Ben Mansour, L. El Mir, J. Mater. Sci.: Mater. Electron. **26**, 1119 (2015).
[15] M. Sreejith, D. Deepu, C. S. Kartha, K. Rajeevkumar, K. Vijayakumar, Appl. Phys. Lett. **105**, 202107 (2014).
[16] J. Zhang, B. Long, S. Cheng, W. Zhang, Int. J. Photoenergy **2013**, 6 (2013).
[17] Y. M. Ko, R. Chalapathy, L. Larina, B. T. Ahn, Cryst. Eng. Comm. **19**, 5764 (2017).
[18] G. G. Kumar, K. Reddy, K. S. Nahm, N. Angulakshmi, A. M. Stephan, J. Phys. Chem. Solids **73**, 1187 (2012).
[19] T. S. Reddy, M. S. Kumar, RSC Advances **6**, 95680 (2016).
[20] G. G. Ninan, C. S. Kartha, K. Vijayakumar, Sol. Energy Mater. Sol. Cells **157**, 229 (2016).

[21] V. K. Arepalli, J. Kim, Thin Solid Films **666**, 34 (2018).
[22] M. S. Abdel-Latif, W. Magdy, T. Tosuke, A. Kanai, A. Hessein, N. M. Shaalan, K. Nakamura, M. Sugiyama, A. Abdel-Moniem, J. Mater. Sci.: Mater. Electron. **31**, 14577 (2020)
[23] D. Avellaneda, A. Paul, S. Shaji, B. Krishnan, J. Solid State Chem. **306**, 122711 (2021).
[24] M. Nair, C. Lopez-Mata, O. Gomez Daza, P. Nair, Semicond. Sci. Technol. **18**, 755 (2003).
[25] A. Paul, S. Shaji, B. Krishnan, D. A. Avellaneda, Opt. Mater. **120**, 111423 (2021).
[26] W. Wang, G. Wang, G. Chen, S. Chen, Z. Huang, Sol. Energy **148**, 12 (2017).
[27] Y. Sui, Y. Wu, Y. Zhang, F. Wang, Y. Gao, S. Lv, Z. Wang, Y. Sun, M. Wei, B. Yao, L. Yang, RSC Advances **8**, 9038 (2018)
[28] P. Zhao, S. Cheng, Adv. Mater. Sci. Eng. **2013**, 726080 (2013).
[29] V. Mahalakshmi, D. Venugopal, K. Ramachandran, R. Ramesh, J. Mater. Sci.: Mater. Electron. **33**, 8493 (2021).
[30] S. Chamekh, N. Khemiri, M. Kanzari, SN Appl. Sci. **2**, 1507 (2020).
[31] N. Jahan, H. Kabir, H. Taha, M. K. Hossain, M. M. Rahman, M. S. Bashar, A. Amri, M. A. Hossain, F. Ahmed, J. Alloys Compd. **859**, 157830 (2021).
[32] T. Raadik, M. Grossberg, J. Krustok, M. Kauk-Kuusik, A. Crovetto, R. Bolt Ettlinger, O. Hansen, J. Schou, Appl. Phys. Lett. **110**, 261105 (2017)
[33] N. Aihara, H. Araki, K. Tanaka, Phys. Status Solidi B **255**, 1700304 (2018)
[34] B. Xu, Y. Zhao, A. Sun, Y. Li, W. Li, X. Han, J. Mater. Sci.: Mater. Electron. **28**, 3481 (2017).
[35] S. Dias, S. Krupanidhi, AIP Advances **6**, 025217 (2016).
[36] Z. Jia, Q. Chen, J. Chen, T. Wang, Z. Li, X. Dou, RSC Advances **5**, 28885 (2015).
[37] S. Thiruvenkadam, P. Sakthi, S. Prabhakaran, S. Chakravarty, V. Ganesan, A. L. Rajesh, Phys. B: Condens. Matter. **538**, 8 (2018).
[38] M. Gusain, P. Rawat, R. Nagarajan, RSC Advances **5**, 43202 (2015).
[39] U. Chalapathi, Y. K. Kumar, S. Uthanna, V. S. Raja, Thin Solid Films **556**, 61 (2014).
[40] D. Alagarasan, S. Varadharajaperumal, K. D. A. Kumar, R. Naik, S. Umrao, M. Shkir, S. AIFaify, R. Ganesan, Opt. Mat. **121**, 111489 (2021).
[41] S. H. Chaki, M. D. Chaudhary, M. P. Deshpande, Adv. Nat. Sci.: Nanosci. Nanotechnol. **5**, 045010 (2014).
[42] P. Fernandes, P. Salomé, A. Da Cunha, J. Phys. D Appl. Phys. **43**, 215403 (2010).
[43] P. Fernandes, P. Salomé, A. Da Cunha, Physica Status Solidi C **7**, 901 (2010).
[44] S. R. Kodigala, Thin film solar cells from earth abundant materials, Elsevier, 1 (2013).
[45] S. Feldmann, M. K. Gangishetty, I. Bravić, T. Neumann, B. Peng, T. Winkler, R. H. Friend, B. Monserrat, D. N. Congreve, F. Deschler, J. Am. Chem. Soc. **143**, 8647 (2021).
[46] M. Wang, K. Wang, Y. Gao, J. I. Khan, W. Yang, S. De Wolf, F. Laquai, Solar RRL **5**, 2100029 (2021).
[47] M. R. Pallavolu, C. D. Kim, V. R. M. Reddy, S. Gedi, C. Park, Sol. Energy. **188**, 209 (2019).
[48] J. Jiang, L. Zhang, W. Wang, R. Hong, Ceram. Int. **44**, 11597 (2018).
[49] E. S. Hossain, P. Chelvanathan, S. A. Shahahmadi, M. T. Ferdaous, B. Bais, S. K. Tiong, N. Amin, Chalcogenide Lett. **15**, 499 (2018).
[50] N. Ravindra, P. Ganapathy, J. Choi, Infrared Phys. Technol. **50**, 21 (2007).
[51] N. A. Bakr, Z. T. Khodair, H. I. Mahdi, Int. J. Mater. Sci. **5**, 261 (2016).
[52] R. Su, Z. Xu, J. Wu, D. Luo, Q. Hu, W. Yang, X. Yang, R. Zhang, H. Yu, T. P. Russell, Q. Gong, Nat. Commun. **12**, 2479 (2021).
[53] M. AlKhalifah, I. El Radaf, M. El-Bana, J. Alloys Compd. **813**, 152169 (2020).
[54] J. Raj Mohamed, L. Amalraj, J. Asian Ceram. Soc. **4**, 357 (2016).
[55] A. Alsaad, A. Ahmad, I. Qattan, Q. M. Al-Bataineh, Z. Albataineh, Crystals **10**, 252 (2020).

*Corresponding author: ilhan.candan@dicle.edu.tr